IOP Conference Series: Materials Science and Engineering

PAPER • OPEN ACCESS

Ductility assessment of a 17-4PH steel through simple multiaxial tests

To cite this article: G Cortis *et al* 2023 *IOP Conf. Ser.: Mater. Sci. Eng.* **1275** 012037

IOP Conf. Series: Materials Science and Engineering 1275 (2023) 012037 doi:10.1088/1757-899X/1275/1/012037

Ductility assessment of a 17-4PH steel through simple multiaxial tests

G Cortis, G B Broggiato and L Cortese

Sapienza Università di Roma, Department of Mechanical and Aerospace Engineering, Via Eudossiana 18, 00184 Rome, Italy

gabriele.cortis@uniroma1.it

Abstract. The present work summarizes the results of an experimental campaign aimed at assessing the ductility of a wrought 17-4PH steel alloy. A simple specimen reproducing multiaxial stress states through a universal testing machine is selected. A Finite Element Model (FEM) for each test is setup to extract the local values of stress and strain in the most critical point on the onset of failure. A Digital Image Correlation (DIC) technique is employed to assess the strain field estimated via FEM. The collected data are used to analyse the material ductility, calculating the triaxiality and deviatoric parameter at the fracture strain. The proposed tests fall in the range of low triaxialities, which are less investigated in the literature. The results obtained are compared with the prediction of a damage model, previously calibrated on the material through more conventional tests. The prediction accuracy of the damage model was fully confirmed by the outcome of the new tests. Eventually, the possibility of replacing some of the conventional tests used for calibration with the proposed specimen is explored.

1. Introduction

Ductility is the ability of a material to sustain appreciable plastic strain before failure, thus its proper estimation combined with the evaluation of ultimate strength are crucial in mechanical design. In the last decades, different ductile damage models have been developed to describe how a material gets damaged with plastic strain and to predict the onset of failure. In literature, different damage models have been developed and can be classified according to their driving principle: Continuum Damage Mechanics-based models (CDM) predict collapse based on thermodynamic principles [1,2], porosity-based models analyse the failure by investigating the evolution of micro-voids, from nucleation to coalescence considering the presence of inclusion sites also [3,4], void-growth-based models link the failure to the evolution of microstructure [5,6], empirical-based models predict failure based only on experimental evidence [7,8]. In the present work only the last will be considered.

For all models, a calibration procedure involving different experimental tests on the specific material is required, which include tensile tests on round smooth or notched bar, torsion or compression tests, and often multiaxial tests, which usually require special testing setups. This means that the calibration procedure is generally non-trivial and not suitable for design companies which could not have in many cases the specific equipment at their disposal. The use of damage models as failure criteria can be applied in different scenarios: estimation of the ultimate strength of the material, evaluation of damage level of a component subjected to residual stress produced by manufacturing processes, investigation of plastic formability limits in forming processes, better knowledge of the behaviour of a material subjected to overloads, evaluating if components can withstand the accidental load without reaching failure.

The aim of the work is basically to assess the effectiveness of a simple specimen geometry, capable to induce multi-axial states of stress, to simplify the experimental phase necessary for the damage models calibration procedure. The specimen geometry proposed by L. Driemeier [9,10] is selected, to be tested employing a common universal testing machine; its dimensional details can be varied to reproduce several multiaxial stress states, ranging from pure shear to different combinations of tension and shear.

Along with the experimental tests of multiaxial specimens, finite element simulations of the experiments and a white light speckle digital image correlation technique are used to evaluate local values of the stress and strain states which cannot be directly measured. Using the collected data coming from the new simple tests, a ductile damage model is calibrated, and compared with the same model previously tuned using typical tests such as round bar, round notched bars, torsion and flat grooved plane strain tests [11]. The new calibration through multiaxial tests compared to the one with conventional tests proved to be equivalent, thus verifying the potential of the new geometry in replacing some of the above mentioned conventional tests. In addition, the good prediction accuracy of the ductile damage model was further confirmed.

2. Theoretical background

While first empirical damage models described damage as a function of triaxiality T only, equation (1) [12,13], recently it was found that damage accumulation also depends on a second parameter [14-17] called Lode Angle θ described by equation (2), which is often expressed in the form of a deviatoric parameter X as in equation (3). The terms I_1, J_2 and J_3 are the first invariant of the stress tensor, the second and third invariant of the deviatoric tensor respectively. In this framework, the triaxiality and the deviatoric parameter fully describe the stress state. According to the latest empirical models, ductile damage is represented by a scalar D that increases proportionally with the equivalent plastic deformation ε_p weighted on a function of the stress state $f(T,X)$, as in equation (4). The parameter D falls in the range from 0 to 1 where D equal to 1 corresponds to the onset of material failure, namely when ε_p assumes the critical value of the equivalent plastic strain to failure ε_f.

$$T = \frac{1}{3}\frac{I_1}{\sqrt{3J_2}} \tag{1}$$

$$\theta = \frac{1}{3}\arccos X \qquad 0 \le \theta \le \pi/3 \tag{2}$$

$$X = \frac{27}{2}\frac{J_3}{(\sqrt{3J_2})^3} \qquad -1 \le X \le 1 \tag{3}$$

$$D = \int_0^{\varepsilon_f} f(T,X)\,d\varepsilon_p \qquad 0 \le D \le 1 \tag{4}$$

Assuming the hypothesis of proportional loading conditions, which means T and X constant with the evolution of plastic strain, posing $D=1$ and inverting the equation (4), the following expression can be obtained (5):

$$\varepsilon_f = f^{-1}(T,X) \tag{5}$$

the above expression graphically represents a surface in the space (T, X, ε_f) usually called “Fracture Surface”, which uniquely links each single stress state, namely each pair of T and X, to a single fracture strain value. Generally, T and X are not perfectly constant, exhibiting limited variations, therefore it is

IOP Conf. Series: Materials Science and Engineering 1275 (2023) 012037 doi:10.1088/1757-899X/1275/1/012037

accepted to use their average value calculated via equations (6-7) to meet the proportional or quasi-proportional loading conditions and allowing the use of expression (5).

$$T_{avg} = \frac{1}{\varepsilon_f}\int_0^{\varepsilon_f} T(\varepsilon)\, d\varepsilon_p \tag{6}$$

$$X_{avg} = \frac{1}{\varepsilon_f}\int_0^{\varepsilon_f} X(\varepsilon)\, d\varepsilon_p \tag{7}$$

Several expressions of the function $f^{-1}(T, X)$ were devised in the literature; in the present work the formulation proposed by Coppola-Cortese-Folgarait (CCF) was adopted (8):

$$\varepsilon_f = \frac{1}{c_1} e^{-c_2 T} \left(\frac{\cos\left[\beta\frac{\pi}{6} - \frac{1}{3}arccos(\gamma)\right]}{\cos\left[\beta\frac{\pi}{6} - \frac{1}{3}arccos(X\gamma)\right]} \right)^{\frac{1}{n}} \tag{8}$$

where c_1, c_2, β e γ are material constants that define the surface shape and n represents the strain hardening exponent of the Hollomon's power law $\sigma=K\varepsilon^n$.

The calibration constants are obtained by means of the following procedure: enough experimental tests characterised by different loading conditions are conducted, typically tensile tests using round bar (RB) and round notched bar (RNB), tensile test in plane strain condition (PS) with flat grooved specimens and torsion tests with cylindrical bar (Tors) [18-20]. For each test, global quantities such as load and displacement are measured and recorded. Subsequently, a Finite Element Analysis (FEA) is performed for each test to derive the local quantities at the critical point of the specimen at the onset of failure, such as the three principal stresses and the equivalent plastic strain, from which T and X were derived through the equations (6-7). Then, a specific set of three parameters (T_{avg}, X_{avg}, ε_f) is obtained for every test at the onset of failure which represents a point in space (T, X, ε_p). Through a minimisation algorithm, the calibration constants governing the shape of the fracture surface are determined: the input data of the algorithm are the coordinates of each point, and the output are the values of the calibration constants that provide the best fit between the fracture surface and the experimental points. For the sake of brevity, please refer to the results section to see the representation of the fracture surface of the steel 17-4PH.

3. Methods and setup

A 17-4PH steel was taken as the reference material since it was already fully characterized by some of the authors of this paper [11] in order to use the results of the previous experimental campaign as a benchmark for the comparison between the fracture surface obtained with the conventional specimens (RB, RNB, PS, Tors) and that obtained employing the proposed multiaxial specimens. All 17-4PH specimens mentioned in this work were manufactured from the same wrought bars used for the previously mentioned work. The material is considered isotropic and its constitutive law is given in figure 1, in which the best fit of the Hollomon's power law is reported: the strength coefficient K and the strain hardening exponent n are equal to 1420 MPa and 0.12 respectively. For further information, please refer to [11]. Concerning the new specimens, as above mentioned in the introduction, the geometry taken into account is that proposed by L. Driemeier [9,10], whose dimensions were optimised through a sensitivity analysis carried out by some of the authors of this paper to meet specific design requirements such as: easiness of manufacturing, constant T and X in the critical area, and localization of the highest plastic strain in the centre of the specimen. Please refer to [21] for more information on the optimisation. The specimen shown in figure 2, hereafter referred to as the "Driemeier", permits to generate several stress states in low regime of triaxialities, such as pure shear or a mix of tensile-shear stress, and can be tested employing only a uniaxial testing machine.

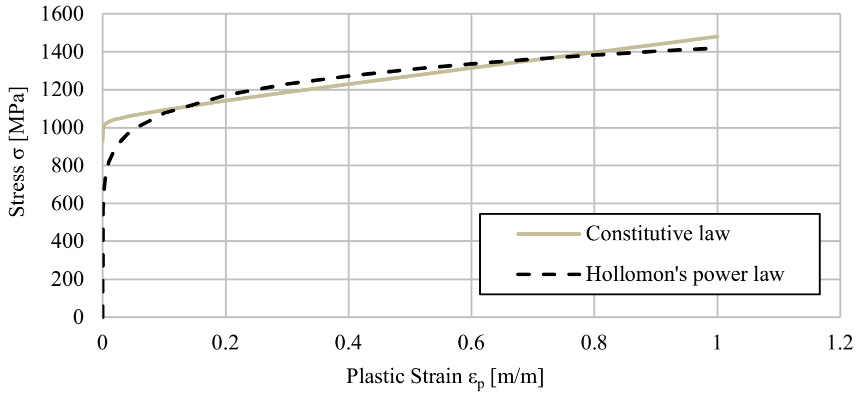

Figure 1. Experimental stress-strain constitutive behavior of 17-4PH wrought steel alloy and corresponding Hollomon’s power law best fit curve.

In particular, the central holes can rotate by an alpha angle (α) along a circumference centred on the centre of the specimen, varying the proportion between shear and tensile state, figure 3a.

In the present work, two different configurations of Driemeier specimens were chosen, having the centres rotated clockwise by 10° and 30° respectively and hereinafter referred as Pos10 and Pos30, figures 3b and 3c. In detail, the Pos30 configuration generates a combination of shear-tensile stress characterized by a higher tensile component than the Pos10 configuration.

The results of the multiaxial tests will be employed to verify the prediction accuracy of the CCF model previously calibrated by conventional tests [11]. In addition, a new calibration will be performed using only the simple multiaxial tests data together with the RB and RNB test results from the previous experimental campaign. The aim is to verify the equivalence between the previously and the new fracture surface and whether it is possible to replace the PS and Tors with the new simple multiaxial tests, which are easier to perform, requiring a more common experimental setup. Finally, a further calibration containing all six tests (RB, RNB, PS, Tors, Pos10, Pos30) will be compared with the others for an additional validation.

The experimental campaign involved three repetitions for both Driemeier specimen configurations and a universal servo-hydraulic MTS with 250 kN maximum load and 150 mm stroke testing machine was used. The same equipment was used for the RB, RNB, PS and Tors tests in the previously experimental campaign [11]. Then, a finite element model was created for both tests using the commercial software ANSYS 2020 R2, to derive the equivalent plastic strain and principal stresses to evaluate the histories T and X with plastic deformation. The mesh size of the models, composed of brick elements, is fine enough to balance numerical accuracy and computational cost. The displacement was applied to the upper part of the specimen, while the lower part was kept fixed. For further validation of the finite element analyses a 2D digital image correlation was carried out to evaluate the full field distribution of the equivalent plastic strain on the specimen surface. The selected DIC software was developed by one of the authors, for more information please refer to [22,23].

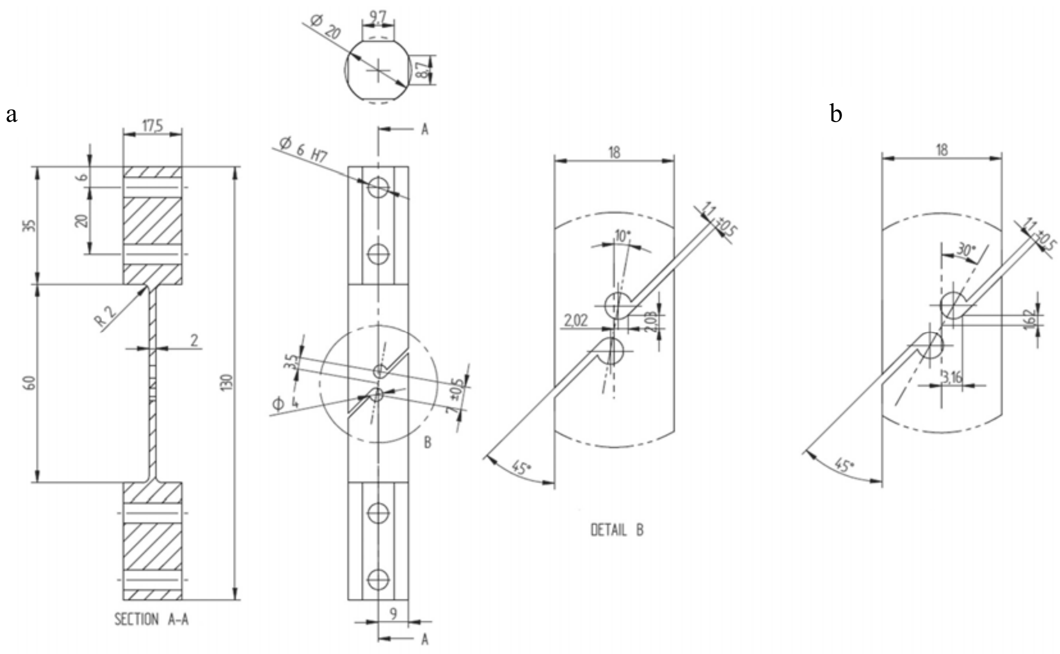

Figure 2. Technical drawings: a) Driemeier 10° (Pos10); b) Driemeier 30° (Pos30).

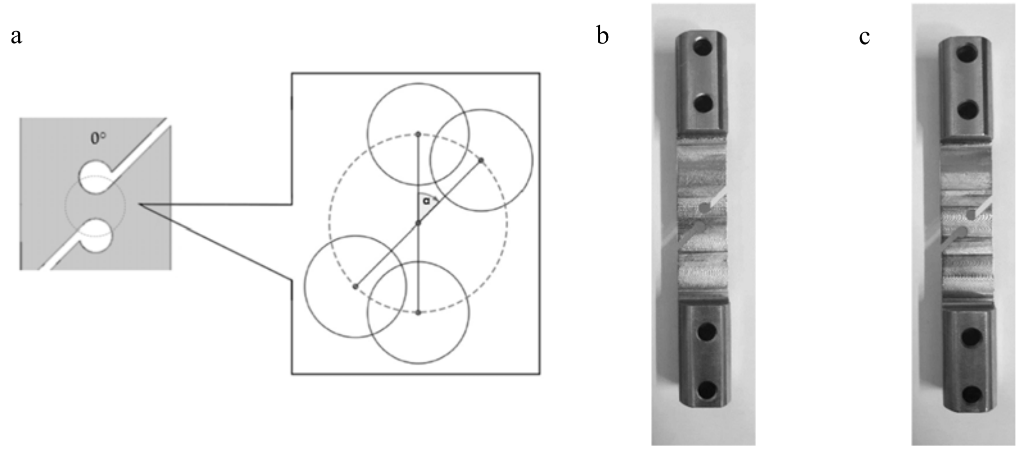

Figure 3. a) Representation of the alpha angle (α); b) Pos10 sample; c) Pos30 sample.

4. Results

The outcome of experimental campaign is reported in figure 4, along with the numerical results of the finite element analyses. Though three repetitions were performed for each specimen, only the average curve was reported. The drop in load-bearing capacity, which indicates the onset failure condition is highlighted by a red circle, and occurred for a displacement of around 0.95 mm for both specimens. The maximum load is around 3.6 kN and 4.0 kN for Pos10 and Pos30 respectively. The experimental-numerical match is very good, which confirmed the reliability of the FE analysis. The accuracy of the FEA was further assessed by comparing the numerically estimated strain field with that evaluated during the experimental test using the 2D-DIC technique, figures 5 and 6. For the sake of simplicity, only the DIC results of the first repetition are reported. As shown for both specimens, Pos10 and Pos30, the distribution of the equivalent plastic strain field is totally comparable. In terms of numerical values the strain estimated through FEA and measured using 2D-DIC technique are essentially equal, with an average value around of 0.33 and 0.46 for Pos10 and Pos30 respectively. This outcome is a further proof the confidence of local quantities retrieved via FEA.

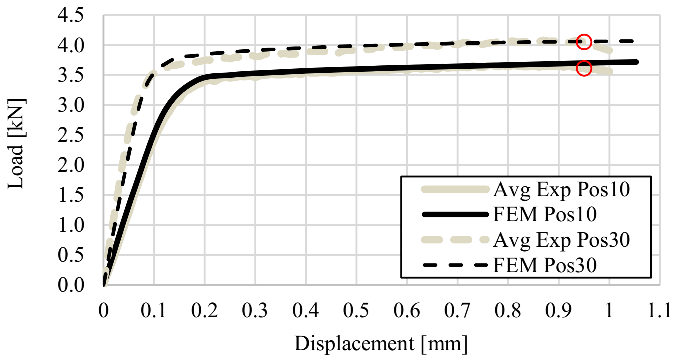

Figure 4. Numerical and experimental load-displacement curves for Pos10 and Pos30 tests. The red circles indicate the onset of failure.

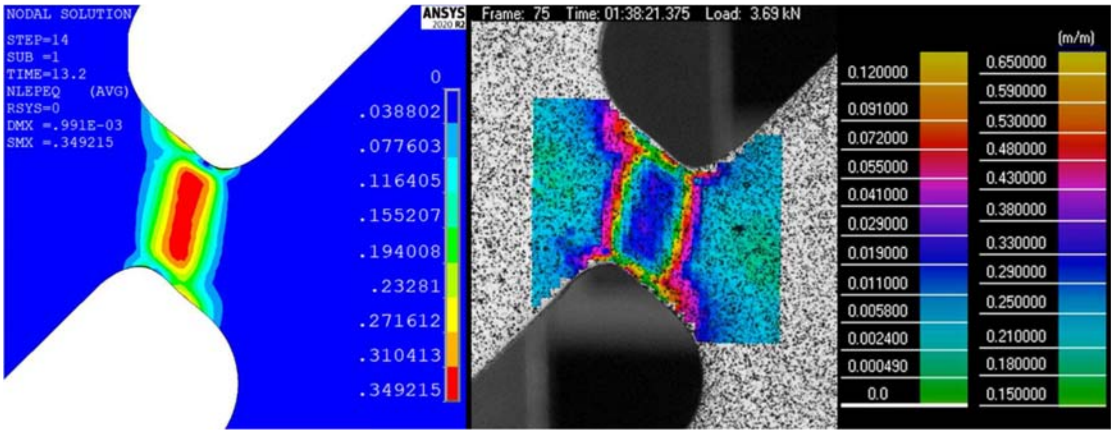

Figure 5. Specimen Pos10: comparison between the strain plastic field evaluated with FEM (left) and DIC technique (right).

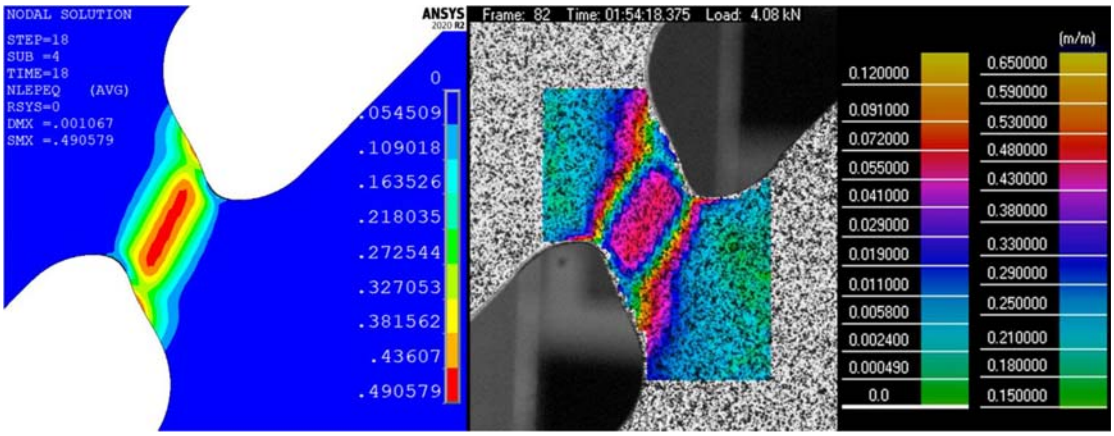

Figure 6. Specimen Pos30: comparison between the strain plastic field evaluated with FEM (left) and DIC technique (right).

IOP Conf. Series: Materials Science and Engineering 1275 (2023) 012037 doi:10.1088/1757-899X/1275/1/012037

Figure 7 illustrates the evolution of the instantaneous value of triaxiality and the deviatoric parameter as a function of equivalent plastic strain: since the quantities exhibit limited variations, their average value up to the onset of failure evaluated by means of equations (6-7) can be taken as a reference. In this way the hypothesis of quasi-proportional loading is met and the fracture surface can be derived according to the equation (5). The value of T_{avg}, X_{avg} and ε_f for both Driemeier specimens are provided in Table 1. For the sake of clarity, the values of the RB, RNB, PS and Tors tests evaluated in the work proposed by Nalli et al. [11] are also reported, which will be employed in the new calibrations involving the Driemeier tests.

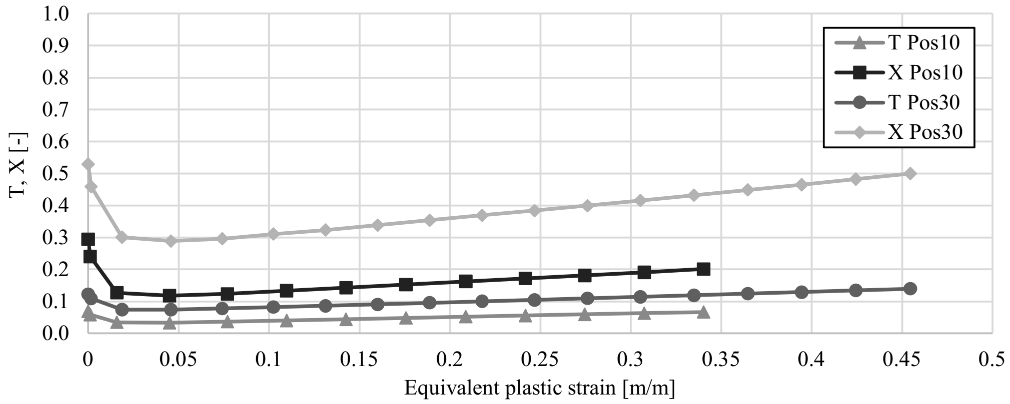

Figure 7. Evolution of the instantaneous values of the triaxiality and deviatoric parameter as function of equivalent plastic strain for Pos10 and Pos30 up to a displacement of 0.95 mm.

Table 1. Values of T_{avg}, X_{avg} and ε_f for multiaxial and conventional specimens.

Tests	T_{avg} [-]	X_{avg} [-]	ε_f [m/m]
Pos10	0.05	0.16	0.33
Pos30	0.10	0.38	0.46
RB	0.61	0.99	1.17
RNB	0.76	0.99	0.81
PS	0.70	0.00	0.66
Tors	0.00	0.00	0.47

Three different calibrations based on data of Table 1 were performed, and the results are illustrated in figures 8a-f. For the sake of clarity, in addition to the 3D graphs, a 2D view of plastic strain as function of triaxiality along X isocurves are provided in figures 8b, 8d and 8f.

In the first calibration conventional specimens are adopted, i.e. RB, RNB, PS and Tors, figures 8a and 8b. The fracture surface was calibrated ex novo. It is clear from figures 8a, 8b that the new Driemeier points, here not used for tuning, are close to the calibrated fracture surface with conventional specimens, meaning that the calibrated damage model well predicts failure under these new loading conditions. It should be noted that the Driemeier test points fall slightly lower than the fracture surface.

A second calibration is based on the new multiaxial specimens Pos10 and Pos30, together with the RB and RNB tests. In this case the two multiaxial specimens replace the PS and Tors specimens, see figures 8c and 8d. The new surface follows the same behaviour as the previous one and is slightly lower because, as already mentioned, the Driemeier specimens exhibited a lower plastic strain at failure. It is worth noting that this new fracture surface presents a good match both with the calibration points and with PS and Tors tests which are excluded from the calibration procedure. Thus, the evidence suggests that the new fracture surface successfully predicts the onset of failure, namely the use of multiaxial specimens does not affect the calibration compared to that performed using conventional specimens.

In the third calibration, reported in figures 8e and 8f, the data coming from all the tests mentioned in Table 1 are involved as input. This calibration is supposed to be the most accurate as it is based on more experimental evidence than the other two. The resulting fracture surface is very close to the experimental points showing a good fit while sharing the same surface behaviour of the other two surfaces.

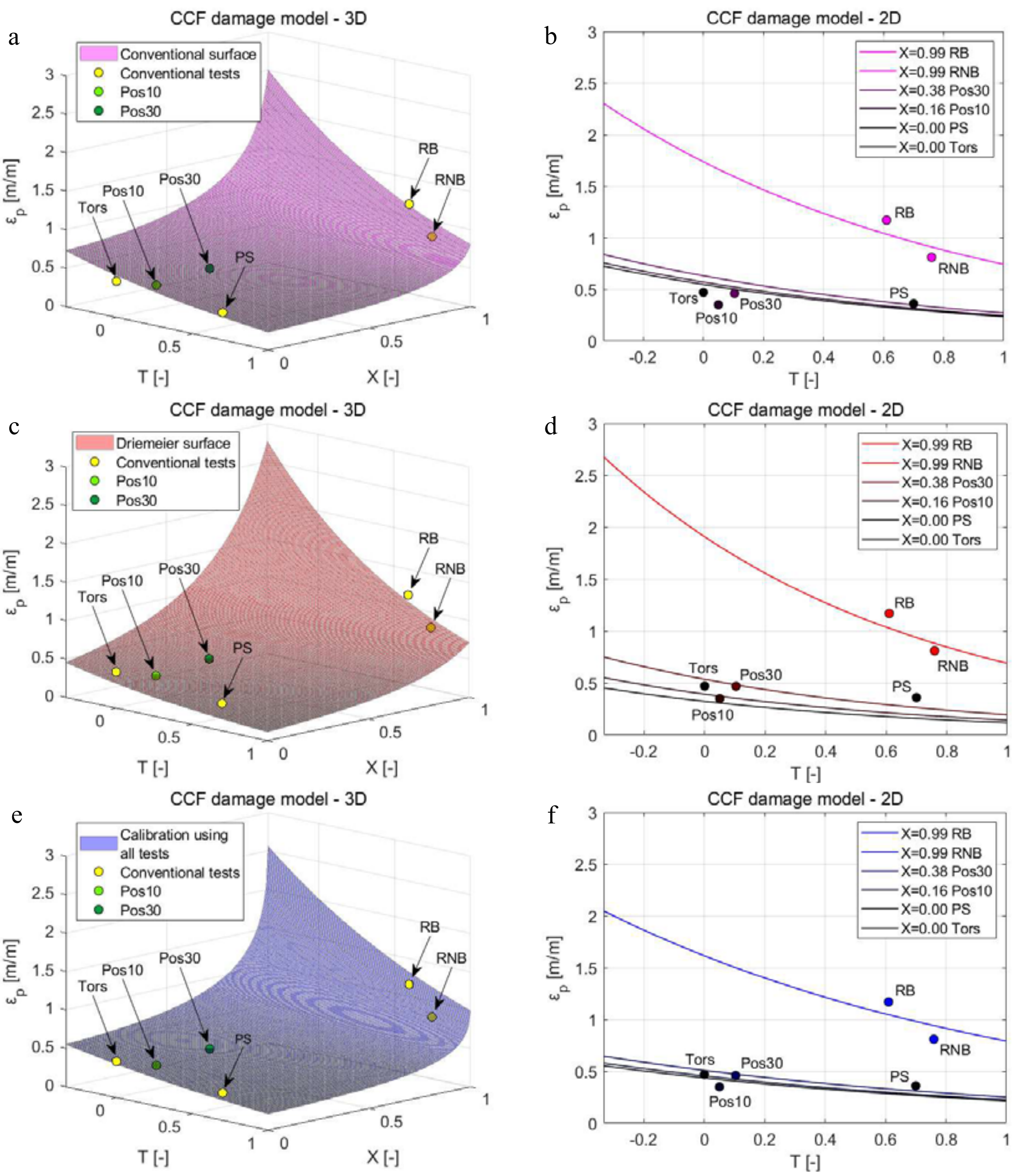

Figure 8. 3D and 2D views of fracture surface of 17-4PH obtained from different set of experimental tests: a-b) Conventional surface involving RB, RNB, PS and Tors; c-d) Driemeier surface involving Pos10, Pos30, RB and RNB; e-f) Surface involving all the tests Pos10, Pos30, RB, RNB, PS and Tors.

Lastly, a comparison of all three surfaces is shown in figure 9; they are very close one another and have the same qualitative behaviour, which means that they can be defined as almost equivalent and it is possible to replace torsion or plane strain tests, with the Driemeier multiaxial tests. Although the two fracture surfaces calibrated with the Driemeier specimens, figures 8c and 8e, are slightly lower than the conventional surface, however they are more conservative regarding the estimation of ductility and then are safety oriented.

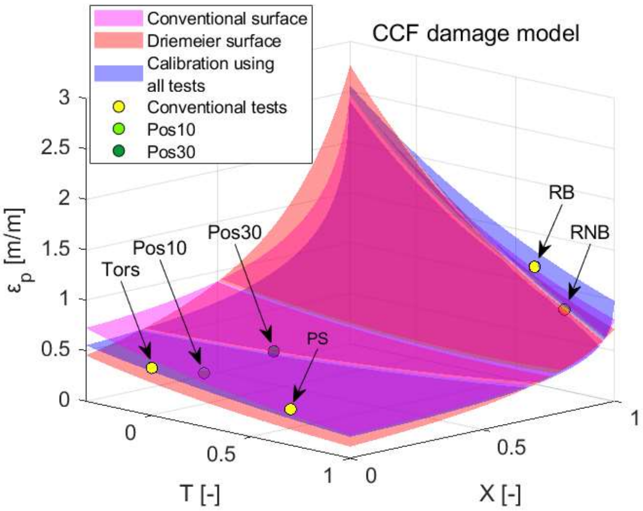

Figure 9. Comparison among the of 17-4PH fracture surfaces obtained by different set of experimental tests.

5. Conclusion

In this work an experimental campaign was carried out to successfully estimate the ductility of a wrought 17-4PH steel alloy. A damage model proposed by one of the authors was tuned to this purpose. In particular, the suitability of adopting simple multiaxial specimens for the tests, compared to more conventional ones, was investigated. The main results reported in the paper showed that together with tensile specimens such as round bars and round notched bars which are also required for elastic-plastic characterisation, it is possible to calibrate a damage model using the proposed multiaxial specimens, replacing more complex geometries, such as cylindrical bar for torsion tests and flat grooved specimens for plane strain conditions tests, thus avoiding more sophisticated testing equipment. All this should lead to a simplification of the calibration procedure, making the use of the damage models on an industrial scale more accessible and widespread. Finally, the new specimen geometry additionally permitted to investigate stress states at low triaxiality, for which few experimental evidences are available in the literature.

References

[1] Lemaitre J 1985 A continuous damage mechanics model for ductile fracture *J. Eng. Mater. Technol.* **107** 83–9
[2] Bonora N 1997 A nonlinear CDM model for ductile failure *Eng. Fract. Mech.* **58** 11–28
[3] Gurson A L 1976 Continuum theory of ductile rupture by void nucleation and growth: Part 1 – Yield criteria and flow rules for porous ductile media *J. Eng. Mater. Technol.* **99** 2-15
[4] Tvergaard V and Needleman A 1984 Analysis of the cup-cone fracture in a round tensile bar *Acta Metall.* **32** 157–69
[5] McClintock F A 1968 A criterion for ductile fracture by growth of holes *J. Appl. Mech.* **35** 363–71

IOP Conf. Series: Materials Science and Engineering 1275 (2023) 012037 doi:10.1088/1757-899X/1275/1/012037

[6] Hancock J W and Mackenzie A C 1976 On the mechanism of ductile failure in high-strength steel subjected to multi-axial stresses *J. Mech. Phys. Solids* **24** 147–69
[7] Cockcroft M G and Latham D J 1968 Ductility and the workability of metals *J. Inst. Metal* **96**
[8] Norris D M Jr, Reaugh J E, Moran B and Quinnones D F 1978 A plastic-strain mean-stress criterion for ductile fracture *J. Eng. Mater. Technol.* **100** 279-86
[9] Driemeier L, Brünig M, Micheli G and Alves M 2010 Experiments on stress-triaxiality dependence of material behavior of aluminum alloys *Mech. Mater.* **42** 207-17
[10] Brünig M, Chyra O, Albrecht D, Driemeier L and Alves M 2008 A ductile damage criterion at various stress triaxialities *Int. J. Plast.* **24** 1731-55
[11] Nalli F, Cortese L and Concli F 2021 Ductile damage assessment of Ti6Al4V, 17-4PH and AlSi10Mg for additive manufacturing *Eng. Fract. Mech.* **241** 107395
[12] Bao Y and Wierzbicki T 2004 On fracture locus in the equivalent strain and stress triaxiality space *Int. J. Mech. Sci.* **46** 81-98
[13] Rice J R and Tracey D M 1969 On the ductile enlargement of voids in triaxial stress fields *J. Mech. Phys. Solids* **17** 201–17
[14] Bai Y and Wierzbicki T 2008 A new model of metal plasticity and fracture with pressure and Lode dependence *Int. J. Plast.* **24** 1071-96
[15] Bai Y and Wierzbicki T 2010 Application of extended Mohr–Coulomb criterion to ductile fracture *Int. J. Fract.* **161**
[16] Dunand M and Mohr D 2014 Effect of Lode parameter on plastic flow localization after proportional loading at low stress triaxialities *J. Mech. Phys. Solids* **66** 133-53
[17] Coppola T, Cortese L and Folgarait P 2009 The effect of stress invariants on ductile fracture limit in steels *Eng. Fract. Mech.* **76** 1288-302
[18] Wierzbicki T, Bao Y, Lee Y W and Bai Y 2005 Calibration and evaluation of seven fracture models *Int. J. Mech. Sci.* **47** 719-43
[19] Kubík P, Šebek F, Hůlka J and Petruška J 2016 Calibration of ductile fracture criteria at negative stress triaxiality *Int. J. Mech. Sci.* **108-9** 90-103
[20] Cortese L, Coppola T, Campanelli F, Campana F and Sasso M 2014 Prediction of ductile failure in materials for onshore and offshore pipeline applications *Int. J. Damage Mech.* **23** 104–23
[21] Cortis G, Nalli F and Piacenti M 2022 A direct methodology for the calibration of ductile damage models from a simple multiaxial test *IOP Conf. Ser.: Mater. Sci. Eng*. **1214** 012016 (online)
[22] Broggiato G B and Cortese L 2009 White-light speckle image correlation applied to large-strain material characterization *Eur. J. Comput. Mech*. /Revue Européenne de Mécanique Numérique **18** 377-92
[23] Broggiato G B, Casarotto L, Del Prete Z and Maccarrone D 2008 Full-field strain rate measurement by white-light speckle image correlation *Eur. J. Comput. Mech.* **18**